Supporting Information for

# Exploring Template-Bound Dinuclear Copper Porphyrin Nanorings by EPR Spectroscopy

Sabine Richert,[1] Jonathan Cremers,[2] Harry L. Anderson,[2] and Christiane R. Timmel [1]*

[1] *Centre for Advanced Electron Spin Resonance (CAESR), Department of Chemistry, University of Oxford, South Parks Road, Oxford, OX1 3QR, United Kingdom.*

[2] *Chemistry Research Laboratory, Department of Chemistry, University of Oxford, Mansfield Road, Oxford, OX1 3TA, United Kingdom.*

*E-mail: christiane.timmel@chem.ox.ac.uk

## Table of Contents

## List of Figures

## List of Tables

# 1 Experimental Details

## 1.1 Sample Preparation

The purity of the compounds was verified by NMR, UV-vis and recycling GPC. An excess of template was added for the preparation of the samples of **c-P10$_{Cu2}$·(T4)$_2$**, **c-P10$_{Cu2}$·(T4$_x$)$_2$** and **c-P10$_{Cu2}$·(T5)$_2$** and complex formation was confirmed by UV-vis spectroscopy. All EPR samples were prepared at concentrations of roughly 0.2 mM in either deuterated or regular toluene. The solutions were subsequently degassed by the freeze-pump-thaw method, backfilled with argon and closed with a subaseal. For storage in liquid nitrogen the subaseal was removed. The frozen samples were directly inserted into the EPR resonator for the measurements at 15 K. The hypothesized structures of all studied samples are shown below.
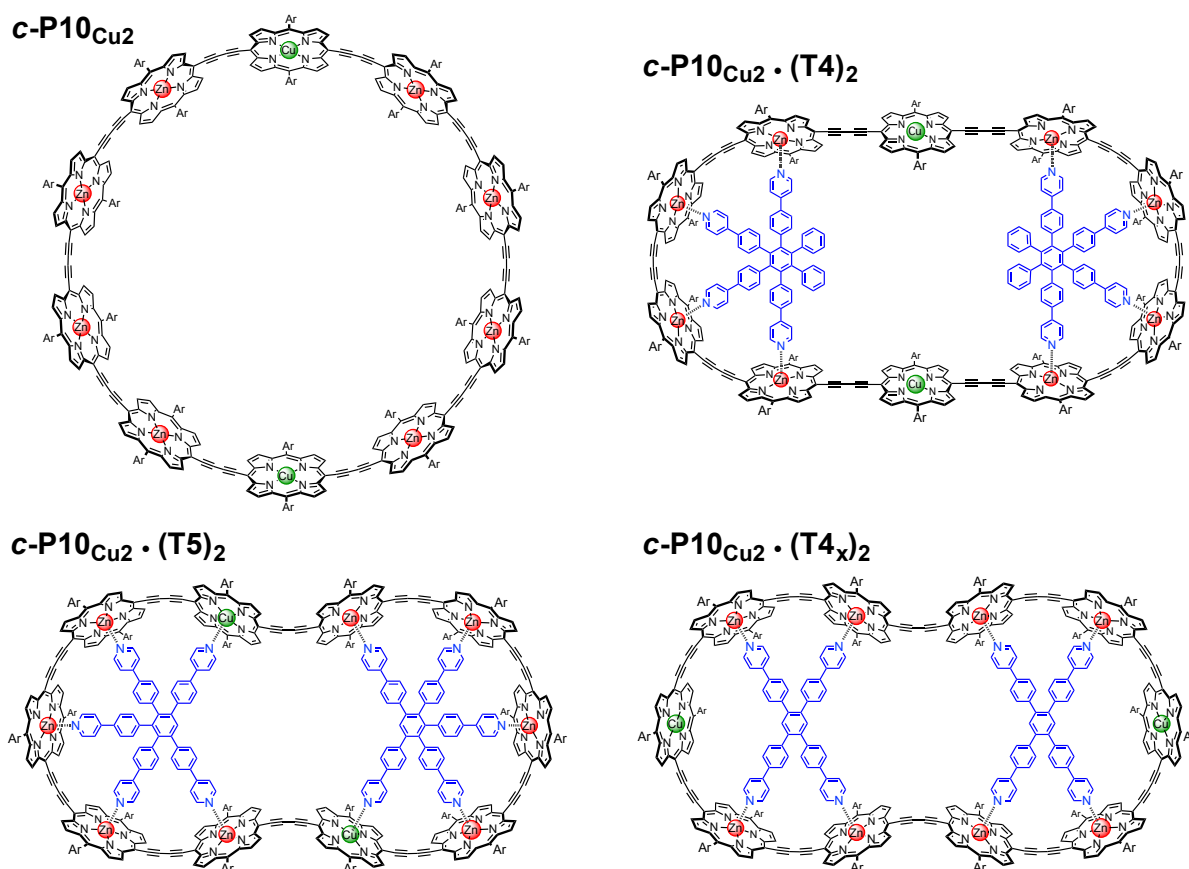


## 1.2 Cw EPR

The continuous wave EPR spectra were recorded on a Bruker EMX spectrometer equipped with a liquid nitrogen flow cryostat. The measurements were performed in frozen toluene-$d_8$ at a temperature of 100 K. The modulation frequency was set to 100 kHz and the modulation amplitude to 5 G at a microwave power of 0.5 mW (26 dB). After data acquisition, the individual spectra were baseline corrected, using the spectrum of pure solvent as a reference to compensate for resonator background signals, normalized and frequency corrected to a common value of 9.39 GHz for direct comparison.

## 1.3 ENDOR

Davies ENDOR measurements at 15 K were carried out at Q-band frequencies (34.0 GHz) on a Bruker ELEXSYS E580 pulsed EPR spectrometer equipped with a Bruker EN 5107D2 resonator and an Oxford Instruments liquid helium flow cryostat (CF935) in order to determine the nitrogen hyperfine and nuclear quadrupole couplings. All experimental ENDOR spectra were obtained using the pulse sequence $\pi - T - \pi/2 - \tau - \pi - \tau -$ echo with $\pi/2$ and $\pi$ pulse lengths of 20 and 40 ns, respectively, and an evolution period $T$ of 27 $\mu$s during which a 25 $\mu$s RF $\pi$ pulse was applied. The inter-pulse delay $\tau$ for the detection sequence was chosen to be 220 ns. The whole echo signal was integrated and recorded as a function of the RF frequency in stochastic mode with an RF increment of 0.1 MHz. The RF power was adjusted based on a nutation experiment.
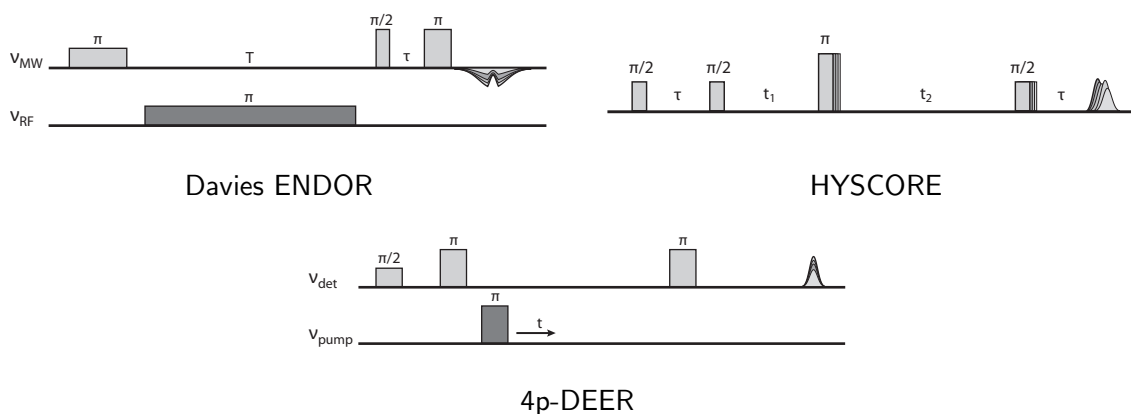


**Figure S1:** Pulse sequences applied in the experiments.

## 1.4 HYSCORE

HYSCORE experiments at 15 K were performed at X-band (Bruker ELEXSYS E680, ER 4118X_MS3 resonator) using the pulse sequence $\pi/2 - \tau - \pi/2 - t_1 - \pi - t_2 - \pi/2 - \tau -$ echo as shown in **Figure S1**. The $\pi/2$ and $\pi$ MW pulses had a length of 16 ns. $t_1$ and $t_2$ were incremented in steps of $dt = 8$ ns starting at $t_1 = t_2 = 64$ ns and a data matrix of $400 \times 400$ points was collected. For every sample, three data sets with $\tau$ values of 140, 216, and 284 ns, respectively, were recorded (and added after data treatment) to compensate for blind-spots. A 4-step phase cycle was applied to remove unwanted echos. The HYSCORE spectra were recorded at a field position corresponding to the maximum of the field-swept EPR spectrum (330 mT $\hat{=}$ $xy$).

After data collection, the spectra were treated in MATLAB [1]. A third-order polynomial baseline correction was applied to all time traces, which were then subjected to apodization with a Hamming window and zero-filled to 1024 points before a 2D Fourier transformation was carried out. The experimental spectra shown in the main text correspond to the absolute-value spectra obtained after Fourier transformation.

Since the deuterium modulations strongly dominated the ESEEM time traces when working with samples in deuterated toluene, all HYSCORE experiments were carried out on samples in regular toluene.

## 1.5 DEER

DEER experiments were performed at 15 K and Q-band frequencies on a Bruker ELEXSYS E580 spectrometer equipped with a Bruker EN 5107D2 resonator and a liquid helium flow cryostat using the sequence $\pi/2 - \tau_1 - \pi - \tau_1 - \tau_2 - \pi - \tau_2 - $ echo at the detection frequency $\nu_{det}$ while applying a single $\pi$ pulse at the pump frequency $\nu_{pump}$ during the interval $\tau_1 - \tau_2$ as shown in **Figure S1**. The pump $\pi$ pulse position was varied step-wise starting at a time $t_0 < \tau_1$ after the first detection $\pi$ pulse up to a time $t < \tau_1 + \tau_2$, shortly before the second $\pi$ pulse at $\nu_{det}$.

Pulse lengths of 12 ns were chosen for all pulses. A 16-step phase cycle needed to be employed to remove unwanted echos (AWG, coherent source). Deuterium nuclear modulations were averaged by increasing $\tau_1$ in eight steps of 16 ns, typically starting at $\tau_1 = 160$ ns. To record the traces shown in the main text, the pump frequency was set to the maximum of the field-swept EPR spectrum ($xy$) and the detection frequency was $\nu_{det} = \nu_{pu} + 100$ MHz. The pump pulse position was varied in steps of either 12 (**c-P10$_{Cu2}$·(T4)$_2$**, **c-P10$_{Cu2}$·(T5)$_2$**) or 16 ns (**c-P10$_{Cu2}$**, **c-P10$_{Cu2}$·(T4$_x$)$_2$**) and data were collected at a repetition rate of 3 $\mu$s for roughly 6 hours using $\tau_2$ values between 1.5 and 4.5 $\mu$s.

The experimental DEER data shown in the main text were background corrected using an exponential background function with a dimensionality of $d = 3$. The corresponding un-corrected curves are shown for reference in **Figure S12**.

## 2  Supplementary Data and Simulations for c-P10$_{Cu2}$ Structures

### 2.1  UV-vis

**Figure S2** shows the room temperature UV-vis spectra of the three investigated samples in deuterated toluene. Upon binding of the template the electronic transitions within the spectral region of the porphyrin Q-bands are considerably red-shifted and become more structured confirming that the template is bound in the samples of **c-P10$_{Cu2}$·(T4)$_2$** and **c-P10$_{Cu2}$·(T5)$_2$**. No major differences in the UV-vis spectra are observed between the samples with **T4** and **T5** templates.
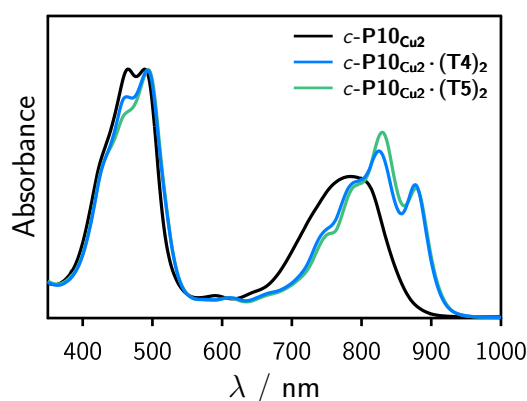


**Figure S2:** UV-vis absorption spectra of the investigated **c-P10$_{Cu2}$** samples in toluene-$d_8$ recorded at 298 K.

To confirm the formation of a 2:1 complex, UV-vis titrations of a solution of **c-P10$_{Cu2}$** were performed with each of the molecular templates **T4**, **T5**, and **T4$_x$**, in chloroform at 298 K. The corresponding data are shown in **Figures S3 to S5**. During the titrations, the porphyrin concentration of 0.96 $\mu$M was kept constant. A red-shift and a characteristic structuring of the Q-bands were observed upon addition of template to a solution of the free **c-P10$_{Cu2}$** ring. In all cases an endpoint of the titration was reached after addition of two equivalents of template.
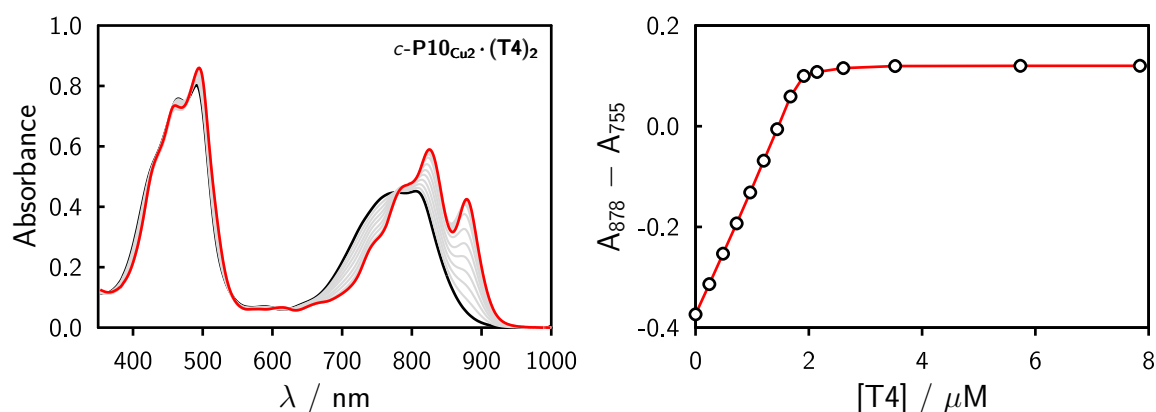


**Figure S3:** UV-vis titration of **c-P10$_{Cu2}$** with **T4** recorded in chloroform at 298 K.
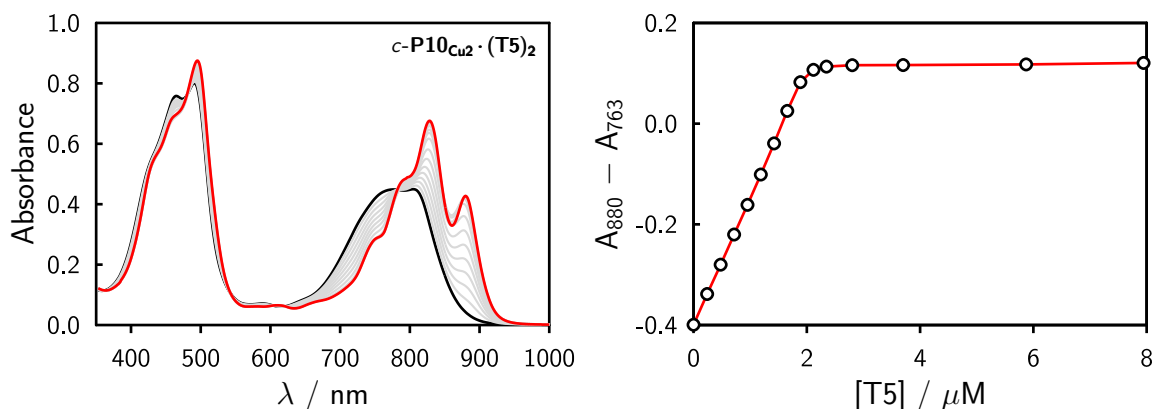
**Figure S4:** UV-vis titration of **c-P10$_{Cu2}$** with **T5** recorded in chloroform at 298 K.
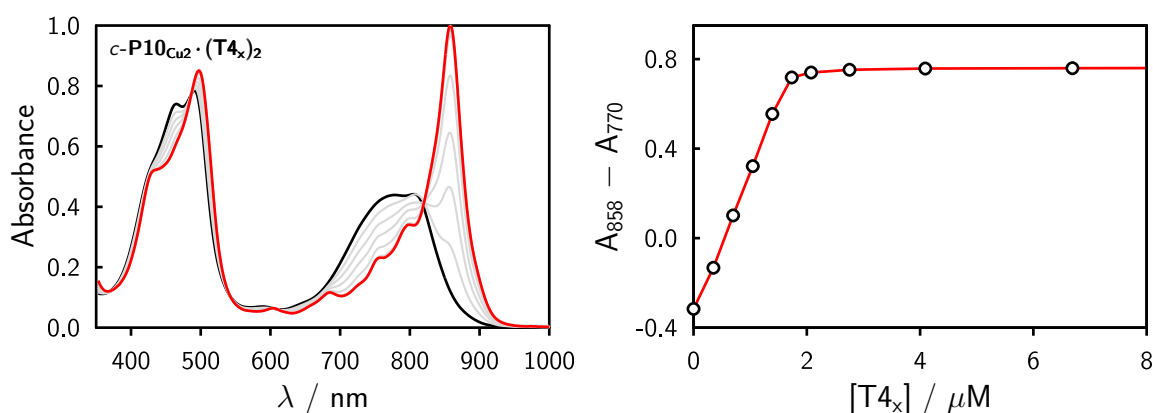


**Figure S5:** UV-vis titration of **c-P10$_{Cu2}$** with **T4$_x$** recorded in chloroform at 298 K.

## 2.2 ENDOR Simulations

Taking the spectrum of **c-P10$_{Cu2}$** as an example, **Figure S6** illustrates the spectral positions at which the ENDOR spectra for the $z$ and $xy$ orientations were taken. For all other samples the field positions were adapted accordingly so that roughly the same part of the spectrum was probed.

The simulations of the $^{14}$N Davies ENDOR spectra were carried out in MATLAB using the software package EasySpin in combination with a home-written fitting routine. The two spectra for each sample corresponding to field positions with contributions mainly from either the $z$- or the $xy$-orientations, were fitted simultaneously. The $g$-values derived from the corresponding cw EPR spectra were kept fixed during the simulations; the microwave frequency, excitation bandwidth and field positions are known from the experiment. Accurate values for the nitrogen hyperfine coupling constants and quadrupolar couplings can be obtained as a result from the fit since the features in the experimental spectra are all well-defined.

In the case of the **c-P10$_{Cu2}$** structures, since the main aim was to determine the relative percentage of the second contribution to the spectra of the template-bound structures, the hyperfine couplings, nuclear quadrupole parameters and $g$-values were taken from numerical simulations of the ENDOR spectra of **P1$_{Cu}$** and **P1$_{Cu}$· py** (cf. **Figures S18 and S19**). Only the relative contribu-
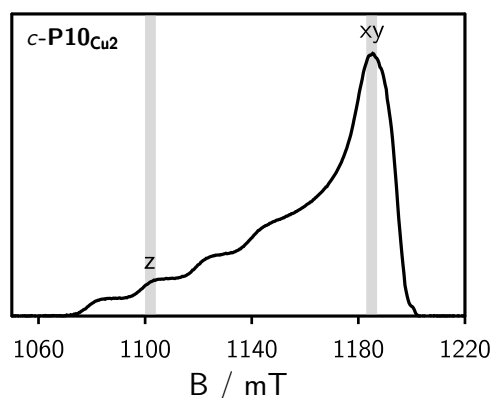
**Figure S6:** Echo-detected field-swept EPR spectrum of **c-P10$_{Cu2}$** recorded at Q-band frequencies. The field positions at which the ENDOR spectra were recorded are indicated.
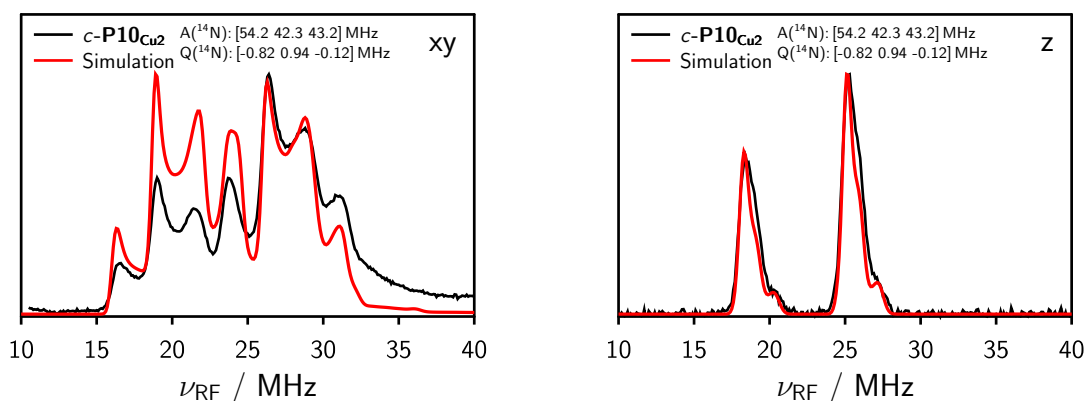


**Figure S7:** $^{14}$N Davies ENDOR of **c-P10$_{Cu2}$** in toluene recorded at field positions corresponding to the *xy* (*left*) and *z* (*right*) orientations together with the corresponding simulations using the values indicated in the figure.

tions of the two components to the spectra of the template-bound samples were varied until the best fit was obtained. The goodness of fit was only judged based on the spectra recorded for the *z*-orientation since the experimental peak intensities for *xy* could not be reproduced satisfactorily in the simulations.

The experimental ENDOR data for the *z* and *xy* tensor orientations together with the corresponding simulations are shown for all three **c-P10$_{Cu2}$** samples in **Figures S7 to S9** and correspond to relative contributions of pyridine-bound copper porphyrin units of $\approx 5\,\%$ and $\approx 30\,\%$ in the samples of **c-P10$_{Cu2}$·(T4)$_2$** and **c-P10$_{Cu2}$·(T5)$_2$**, respectively. All other simulation parameters employed are indicated in the figures.

The differences in the relative line intensities between the experimental and simulated ENDOR spectra in *xy* orientation could be due to the neglect of hyperfine enhancement effects in the simulations. Saturation of the ENDOR lines during measurement was verified experimentally by recording the ENDOR spectra at a 10-times slower repetition rate and comparing the relative line

**Figure S8:** [14]N Davies ENDOR of **c-P10$_{Cu2}$·(T4)$_2$** in toluene recorded at field positions corresponding to the *xy* (*left*) and *z* (*right*) orientations together with the corresponding simulations using the values indicated in the figure. The relative contribution of the second component was $\approx 5\,\%$.
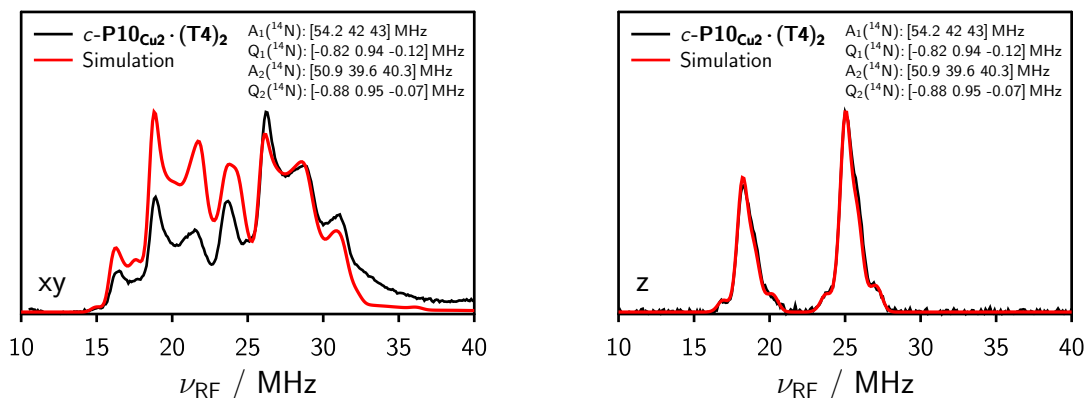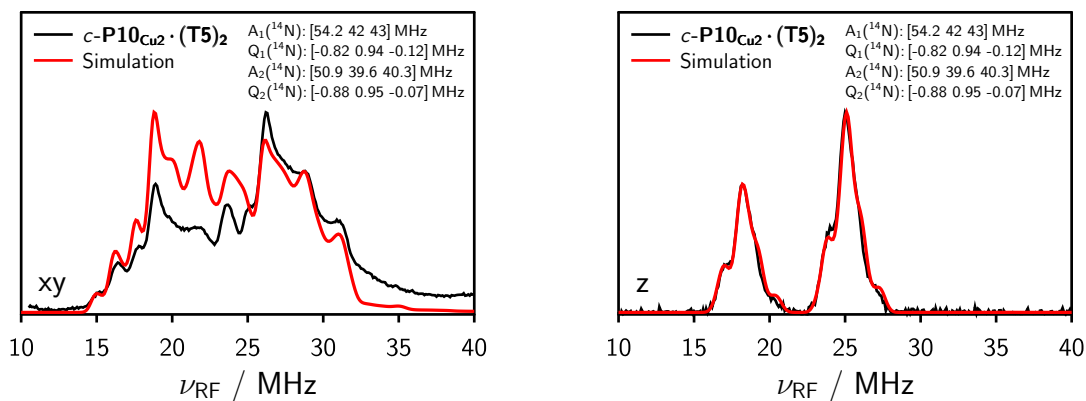


**Figure S9:** [14]N Davies ENDOR of **c-P10$_{Cu2}$·(T5)$_2$** in toluene recorded at field positions corresponding to the *xy* (*left*) and *z* (*right*) orientations together with the corresponding simulations using the values indicated in the figure. The relative contribution of the second component was $\approx 30\,\%$.

intensities. It can be ruled out as a possible cause of the intensity differences as is shown in **Figure S10**.
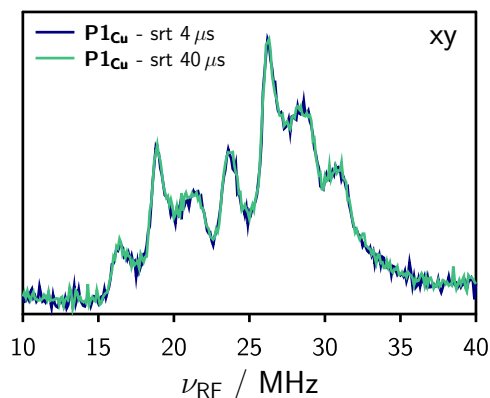
**Figure S10:** $^{14}N$ Davies ENDOR spectra of **P1$_{Cu}$** in toluene recorded at a field position corresponding to the *xy* orientation at two different shot-to-shot repetition rates as indicated.

## 2.3 DEER Simulations and Raw Data

**Figure S11** shows the best fits to the experimental DEER data for all **c-P10$_{Cu2}$** samples from Tikhonov regularization as obtained making use of the corresponding algorithm implemented in DeerAnalysis [2]. Although the fit is not perfect, certainly partially due to the presence of orientation selection in the time traces which cannot be accounted for by this model-free analysis, the main features in the experimental data are well reproduced. The raw data before background correction are shown in **Figure S12** for reference.
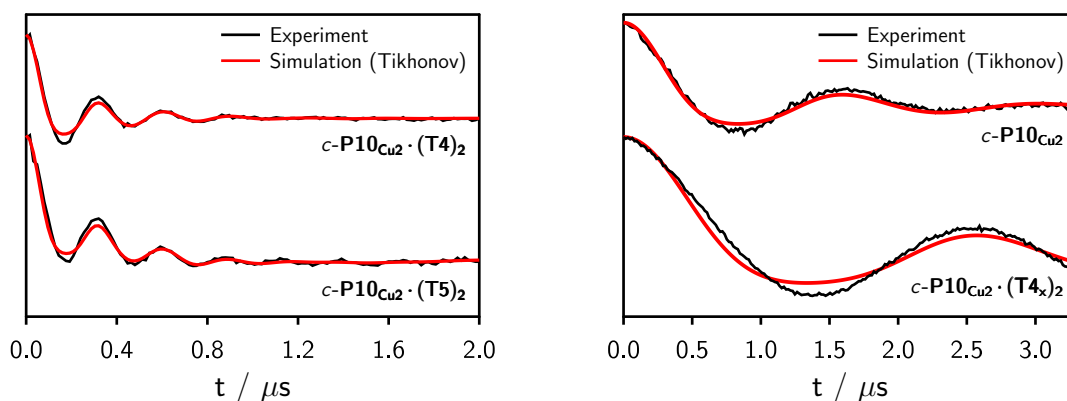


**Figure S11:** Experimental DEER traces for **c-P10$_{Cu2}$·(T4)$_2$** and **c-P10$_{Cu2}$·(T5)$_2$**(*left*) and **c-P10$_{Cu2}$** and **c-P10$_{Cu2}$·(T4$_x$)$_2$** (*right*) together with the corresponding simulations obtained as a result from Tikhonov regularization as implemented in DeerAnalysis.

The use of Tikhonov regularization for analysis of the DEER traces will only yield reliable results if any effects of orientation selection can be neglected. Generally, when exciting and probing in the $g_\perp$ region of the copper spectrum, as was done in the present work, orientation selection can often be neglected, since the perpendicular dipolar splitting frequency is detected in all cases independently of the relative orientation of the two copper centers due to the axial symmetry of the **g**-tensor [3].

To verify experimentally that the effects of orientation selection can safely be neglected in the analysis of the DEER data acquired for the **c-P10$_{Cu2}$** structures at $g_\perp$, DEER traces were recorded at
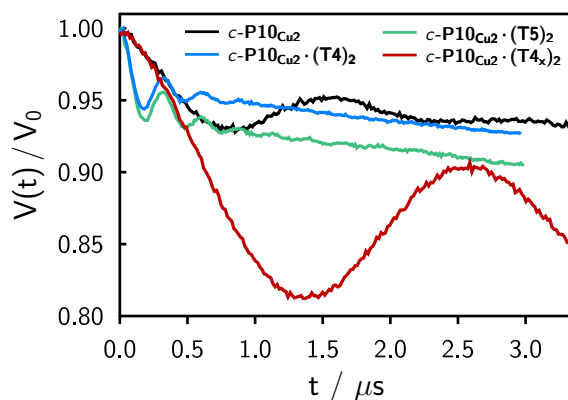
**Figure S12:** Experimental DEER data prior to background correction by an exponential background function with dimensionality $d$ of 3.

different fields and with different frequency offsets within the $g_\perp$ region of the spectrum. Orientation selection is expected to cause differences in the modulation depth, but should not markedly influence the distances and distance distributions in the present case. Exemplary DEER traces for **c-P10$_{Cu2}$** are shown in **Figure S13** together with a field-swept echo-detected EPR spectrum indicating the positions of the detection and pump pulses within the spectrum. In the three different cases shown below, the same dipolar frequencies and indistinguishable distance distributions were obtained within experimental error.
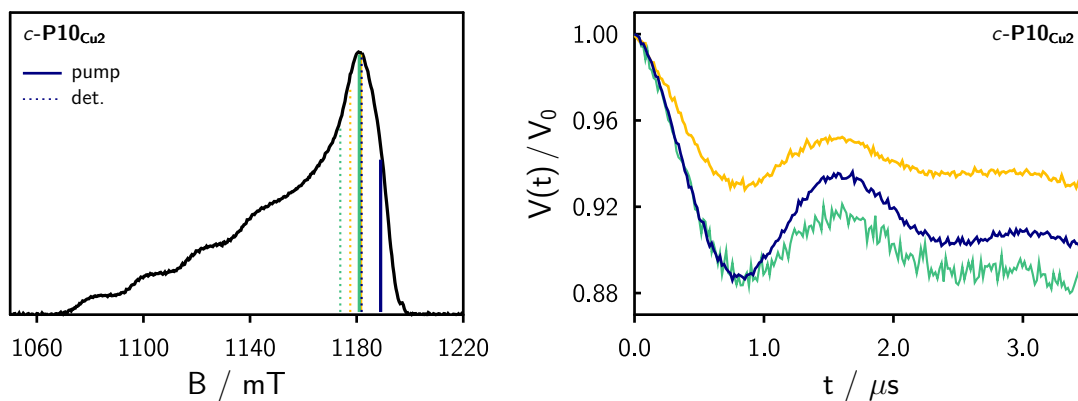


**Figure S13:** Experimental field-swept echo-detected EPR spectrum indicating the pump and detection pulse positions chosen for DEER (*left*) and DEER traces of **c-P10$_{Cu2}$** recorded at different field positions and with different frequency offsets on $g_\perp$.

## 2.4 Molecular Modeling of c-P10$_{Zn10}$·(T5)$_2$

To get an idea about the approximate distances to be expected in the complex of **c-P10$_{Cu2}$·(T5)$_2$** for the limiting case of complete binding of copper to the fifth pyridine template leg, molecular mechanics calculations were carried out on a structure of the ten-membered porphyrin nanoring with ten zinc centers, **c-P10$_{Zn10}$·(T5)$_2$**, using *HyperChem* Version 9. The geometry optimization

was carried out using the MM+ force field with modified parameters adapted for the investigated porphyrin structures [4–7].
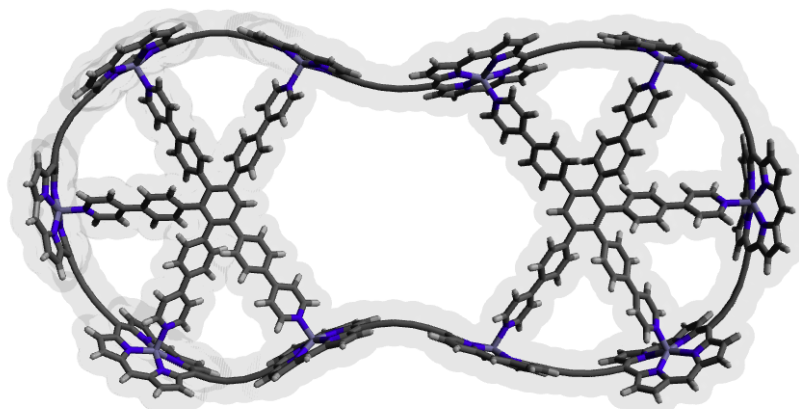


**Figure S14:** Illustration of the optimized molecular structure of **c-P10$_{Zn10}$·(T5)$_2$** obtained as a result from molecular modeling using *HyperChem*.

The average Zn$\cdots$Zn distances in this structure amount to 2.5, 4.3, and 5.0 nm, for the short, intermediate, and long distance, respectively, as mentioned in the main text.

## 3 Investigation of P1$_{Cu}$ and P1$_{Cu}$·py

### 3.1 ENDOR

$^{14}$N Davies ENDOR measurements at Q-band frequencies (34.0 GHz) were carried out at 15 K. **Figure S15** shows a comparison of the ENDOR spectra of **P1$_{Cu}$** and **P1$_{Cu}$·py** in toluene for two different field positions corresponding to the *xy* and *z* orientations, respectively. From the shift of the spectrum to lower values it can clearly be seen that the hyperfine coupling constants of the in-plane nitrogens of the copper porphyrin are reduced upon binding of the pyridine ligand. A field-swept echo-detected EPR spectrum showing the precise field positions at which the ENDOR spectra were taken is shown in **Figure S16**. Since the entire spectrum is shifted (i.e. no residual peaks remain at the original positions), the binding can be assumed to be quantitative in the present case. **Figure S17** gives an exemplary illustration how the peak positions and peak spacings in the ENDOR spectra relate to the magnitude of the hyperfine and nuclear quadrupole couplings. The positions of A$_x$/2, A$_y$/2, and A$_z$/2 are highlighted in gray.

The simulations of the $^{14}$N Davies ENDOR spectra were carried out in MATLAB as described above for the **c-P10$_{Cu2}$·(T5)$_2$** structures. **Figures S18 and S19** show the experimental spectra for **P1$_{Cu}$** and **P1$_{Cu}$·py** together with the respective simulations. The obtained simulation parameters are indicated in the figures.

The values obtained from the simulations are fairly reliable although the relative peak intensities are not reproduced correctly in all cases, since the relevant information about the magnitudes of the couplings is solely contained in the peak positions.

As was discussed in the main text, it is observed that the nitrogen hyperfine coupling constants are reduced by about 3 MHz in all directions upon binding of an axial nitrogen ligand to copper.
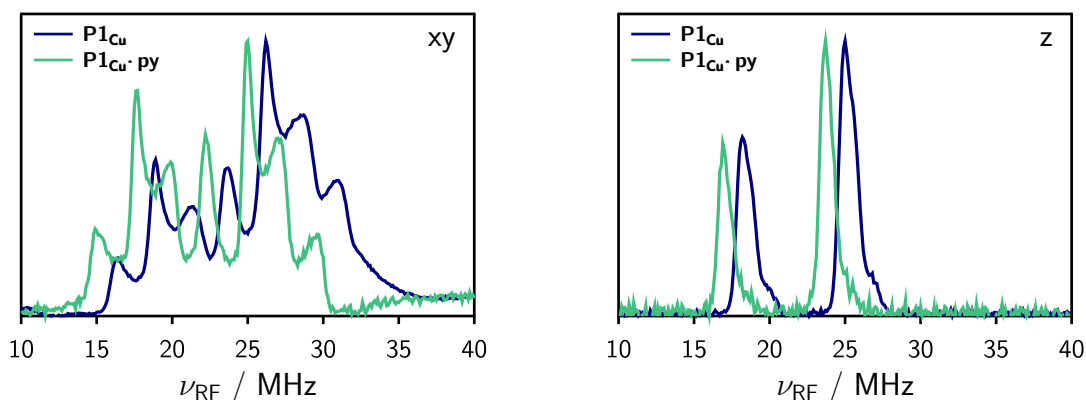
**Figure S15:** $^{14}$N Davies ENDOR of **P1$_{Cu}$** in toluene and **P1$_{Cu}$· py** in toluene:pyridine 1:1 recorded at field positions corresponding to the *xy* (*left*) and *z* (*right*) orientations.
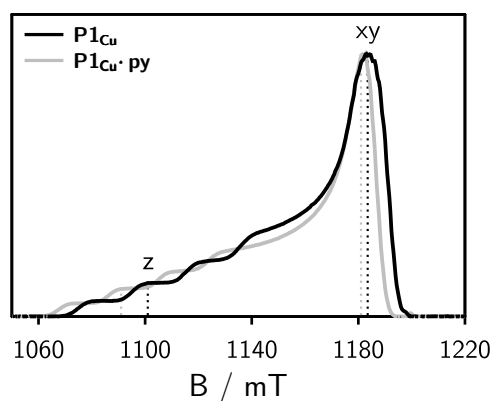


**Figure S16:** Echo-detected field-swept EPR spectra of **P1$_{Cu}$** and **P1$_{Cu}$· py** recorded at Q-band frequencies. The field positions at which the ENDOR spectra where recorded are indicated.
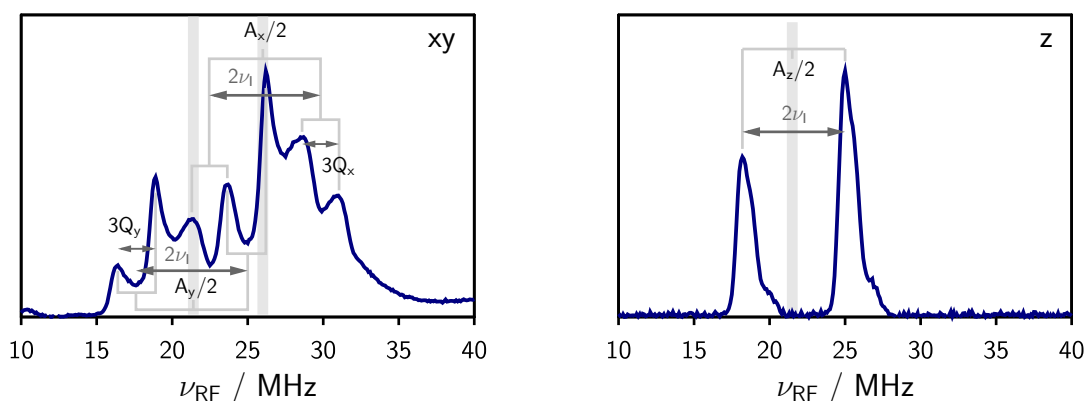


**Figure S17:** Illustration of the peak assignment in $^{14}$N Davies ENDOR shown for experimental spectra of **P1$_{Cu}$** in toluene recorded at field positions corresponding to the *xy* (*left*) and *z* (*right*) orientations.
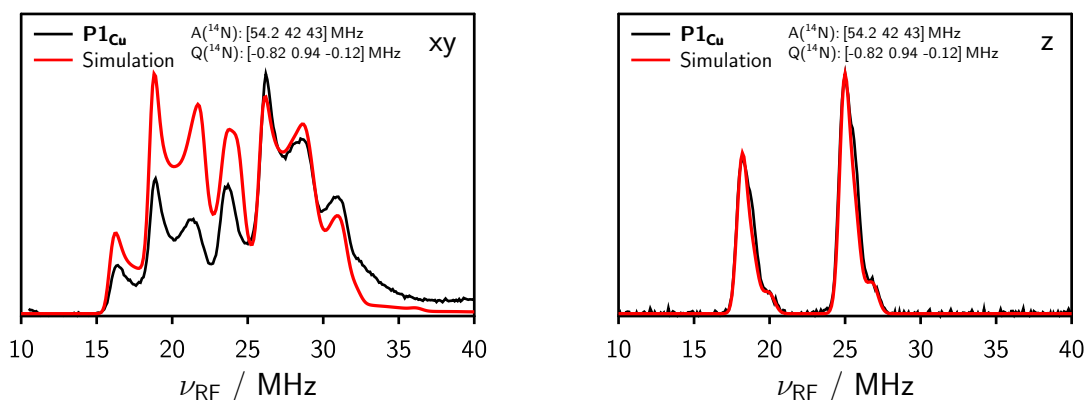
**Figure S18:** $^{14}$N Davies ENDOR of **P1$_{Cu}$** in toluene recorded at field positions corresponding to the *xy* (*left*) and *z* (*right*) orientations together with the corresponding simulations using the values indicated in the figure.



**Figure S19:** $^{14}$N Davies ENDOR of **P1$_{Cu}$·py** in toluene:pyridine 1:1 recorded at field positions corresponding to the *xy* (*left*) and *z* (*right*) orientations together with the corresponding simulations using the values indicated in the figure.
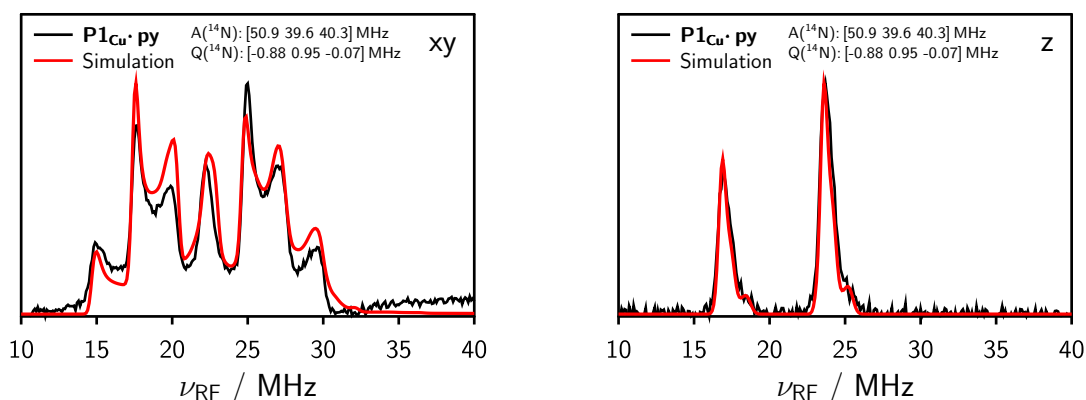
## 3.2 Cw EPR

Also by continuous wave (cw) EPR spectroscopy, the binding of copper to nitrogen ligands can be detected. Major changes in the frozen solution spectra are observed between **P1$_{Cu}$** and **P1$_{Cu}$·py** as shown in **Figure S20**. From a comparison of the spectra it seems that the interaction of copper with a pyridine ligand increases the *g*-values, since the whole spectrum appears to be shifted to lower fields. Also the copper hyperfine couplings seem to be affected as can be seen from the spacing between the two outmost copper transitions at the low-field side of the spectrum.

For a numerical simulation of the cw EPR spectra using EasySpin, the nitrogen hyperfine couplings were taken as determined from ENDOR and kept fixed during the fitting process since the values are known with high precision. All other parameters were varied until a good fit to the experimental data was obtained. Since the ENDOR spectra of **P1$_{Cu}$·py** suggest that the binding of the axial nitrogen ligand to copper is quantitative, also the cw EPR spectra were simulated assuming just
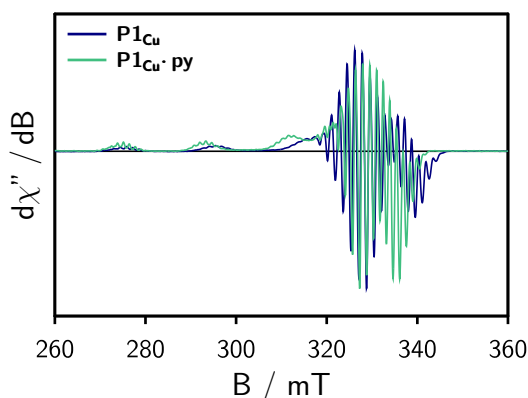
**Figure S20:** Comparison of the baseline corrected continuous wave EPR spectra of **P1$_{Cu}$** and **P1$_{Cu}$· py** taken at X-band (9.5 GHz) in frozen toluene at 100 K.

one component. The experimental spectra together with the corresponding simulations are shown in **Figure S21**. The simulation parameters used are indicated in the figures.
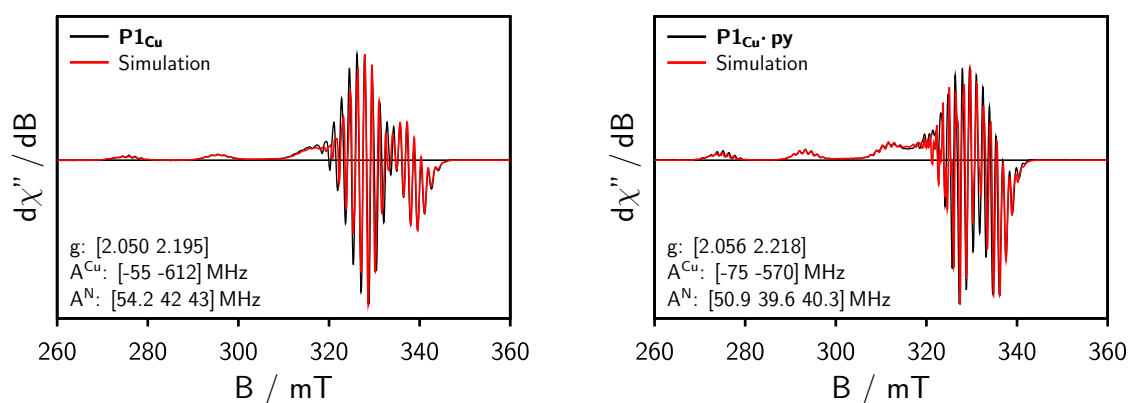


**Figure S21:** Experimental cw EPR spectra for **P1$_{Cu}$** (*left*) and **P1$_{Cu}$· py** (*right*) recorded in frozen toluene at 100 K together with the corresponding simulations carried out using Easyspin. The simulation parameters are indicated in the figure.

It is observed that upon binding of a nitrogen ligand to copper, not only the nitrogen couplings but also the *g*-values and copper hyperfine couplings are altered. A reduction of the *g*-values and an increase in the out-of-plane hyperfine coupling constant of copper, $A_{||}$, have to be assumed in order to reproduce the experimentally observed changes.

The *g*-values and the copper out-of-plane hyperfine coupling constant, $A_{||}$, can reliably be determined from these simulations, whereas the value of the in-plane copper hyperfine coupling constant, $A_{\perp}$, is generally quite uncertain when determined from cw EPR due to a strong overlap of many features in the relevant spectral region. To determine this value with higher precision, a recently published new approach making use of ultra-wideband excitation with frequency-swept chirp pulses could be used [8].

**Table S1** summarizes the experimental parameters obtained from simulations of the ENDOR and cw EPR spectra, which are in good agreement with those reported in the literature for similar

copper porphyrin monomers [9, 10]. The differences in the hyperfine coupling parameters and *g*-values between **P1$_{Cu}$** and **P1$_{Cu}$· py** are comparatively large, illustrating the power of EPR to detect subtle changes in the local environment of the paramagnetic center. The absolute values of the hyperfine coupling constants are thus a very sensitive measure of metal-ligand interactions.

**Table S1:** Overview of the hyperfine coupling parameters and *g*-values obtained from a numerical simulation of the experimental ENDOR and cw EPR spectra of **P1$_{Cu}$** and **P1$_{Cu}$· py**.

|  | $A^N_{[x,\,y,\,z]}$ / MHz | $A^{Cu}_{\|\|}$ / MHz | $[g_\perp, g_{\|\|}]$ |
|---|---|---|---|
| **P1$_{Cu}$** | [54.2, 42, 43] | -612 | [2.050, 2.195] |
| **P1$_{Cu}$· py** | [50.9, 39.6, 40.3] | -570 | [2.056, 2.218] |

# 4  Additional DFT Results

**Figure S22** shows the chosen axis definition and nitrogen assignment in the molecular frame of **P1$_{Cu}$** as referred to in the main text. The **g**-tensor orientations obtained from DFT calculations are depicted within the molecular frames of **P1$_{Cu}$** and **P1$_{Cu}$· py** in **Figure S23**. Additionally, the hyperfine coupling tensors and their orientations are visualized, where the magnitudes of the principle values of the copper hyperfine tensors have been scaled down by a factor of four with respect to the nitrogen and carbon tensors. From the figure it can also be seen that the presence of the pyridine ligand influences the **g**-tensor orientation.
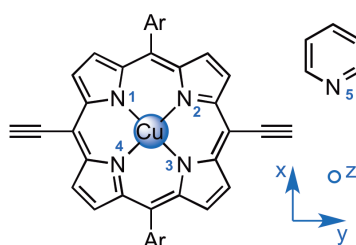


**Figure S22:** Illustration of the definition of the Cartesian axes in the molecular frame of **P1$_{Cu}$**.

**Figure S24** illustrates the orientation and magnitude of the nuclear quadrupole couplings in **P1$_{Cu}$** and **P1$_{Cu}$· py**. With respect to the hyperfine coupling tensors in **Figure S23**, all nuclear quadrupole tensors have been scaled up by a factor of 30. In **Table S2**, the calculated nuclear quadrupole couplings for all nitrogen nuclei in **P1$_{Cu}$** and **P1$_{Cu}$· py** are summarized and compared. It can be seen that the quadrupolar couplings of the pyridine nitrogen are relatively large in comparison with the ones of the in-plane nitrogen nuclei.
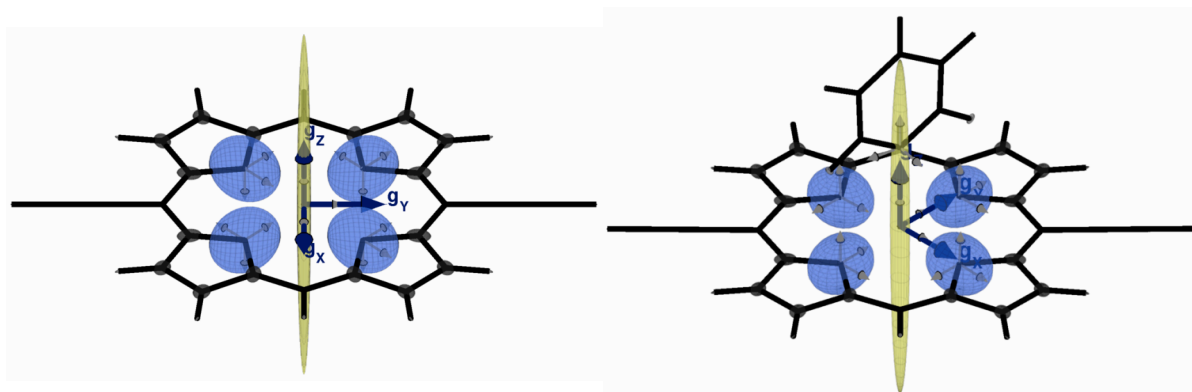
**Figure S23:** Visualization of the hyperfine interaction tensors and **g**-tensor orientations for **P1$_{Cu}$** (*left*) and **P1$_{Cu}$·py** (*right*). Compared to the proton and carbon hyperfine tensors, the magnitude of the principle values of the hyperfine coupling tensors have been scaled down by a factor of two and four in the case of nitrogen and copper, respectively, for better visualization.
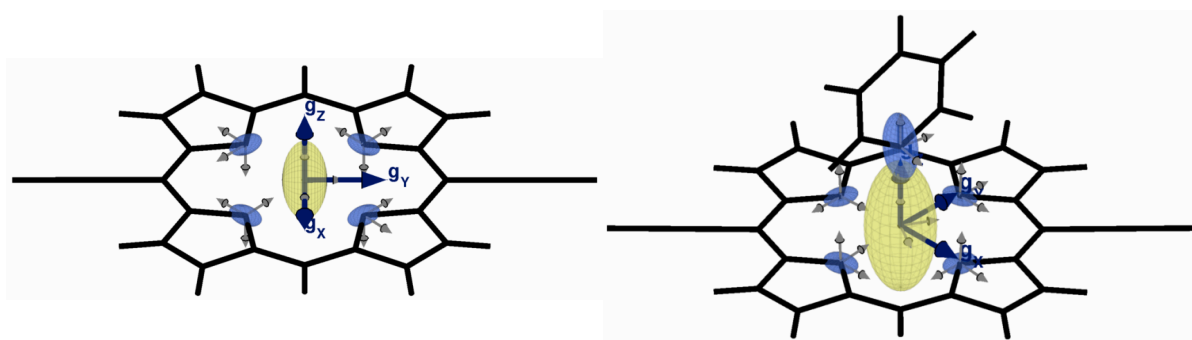


**Figure S24:** Visualization of the nuclear quadrupole tensors in the molecular frame of **P1$_{Cu}$** (*left*) and **P1$_{Cu}$·py** (*right*). With respect to the corresponding hyperfine interaction tensors shown above, the tensor dimensions have been scaled up by a factor of 30.

**Table S2:** Nitrogen quadrupolar coupling constants calculated for **P1$_{Cu}$** and **P1$_{Cu}$·py** with ORCA V 3.0 using DFT/B3LYP in combination with the EPRII basis set.

| | $Q^{N^{1-4}}_{[x, y, z]}$ / MHz | $Q^{N^5}_{[x, y, z]}$ / MHz |
|---|---|---|
| **P1$_{Cu}$** | [-0.70, 1.07, -0.37] | - |
| **P1$_{Cu}$·py** | [-0.80, 1.09, -0.29] | [0.80, 1.30, -2.10] |

# References

[1] MATLAB, *version 7.11.0 (R2010b)*; The MathWorks Inc.: Natick, Massachusetts, 2010.

[2] Jeschke, G.; Chechik, V.; Ionita, P.; Godt, A.; Zimmermann, H.; Banham, J.; Timmel, C. R.; Hilger, D.; Jung, H. DeerAnalysis2006 - a Comprehensive Software Package for Analyzing Pulsed ELDOR Data. *Appl. Magn. Reson.* **2006**, *30*, 473–498.

[3] Bowen, A. M.; Tait, C. E.; Timmel, C. R.; Harmer, J. R. Orientation-Selective DEER Using Rigid Spin Labels, Cofactors, Metals, and Clusters. In *Structural Information from Spin-Labels and Intrinsic Paramagnetic Centres in the Biosciences*; Timmel, C. R., Harmer, J. R., Eds.; Structure and Bonding; Springer: Berlin Heidelberg, 2013; Vol. 152; Chapter 7, pp 283–327.

[4] Marques, H. M.; Cukrowski, I. Molecular Mechanics Parameters for the Modelling of Four-Coordinate Zn(II) Porphyrins. *Phys. Chem. Chem. Phys.* **2003**, *5*, 5499–5506.

[5] Marques, H. M.; Cukrowski, I. Molecular Mechanics Modelling of Porphyrins. Using Artificial Neural Networks to Develop Metal Parameters for Four-Coordinate Metalloporphyrins. *Phys. Chem. Chem. Phys.* **2002**, *4*, 5878–5887.

[6] Goldstein, E.; Ma, B.; Lii, J.-H.; Allinger, N. L. Molecular Mechanics Calculations (MM3) on Nitriles and Alkynes. *J. Phys. Org. Chem.* **1996**, *9*, 191–202.

[7] Jarowski, P. D.; Diederich, F.; Houk, K. N. Structures and Stabilities of Diacetylene-Expanded Polyhedranes by Quantum Mechanics and Molecular Mechanics. *J. Org. Chem.* **2005**, *70*, 1671–1678.

[8] Segawa, T. F.; Doll, A.; Pribitzer, S.; Jeschke, G. Copper ESEEM and HYSCORE through Ultra-Wideband Chirp EPR Spectroscopy. *J. Chem. Phys.* **2015**, *143*, 044201/1–8.

[9] Greiner, S. P.; Rowlands, D. L.; Kreilick, R. W. EPR and ENDOR Study of Selected Porphyrin- and Phthalocyanine-Copper Complexes. *J. Phys. Chem.* **1992**, *96*, 9132–9139.

[10] Finazzo, C.; Calle, C.; Stoll, S.; Van Doorslaer, S.; Schweiger, A. Matrix Effects on Copper(II)phthalocyanine Complexes. A Combined Continuous Wave and Pulse EPR and DFT Study. *Phys. Chem. Chem. Phys.* **2006**, *8*, 1942–1953.